RSC Advances

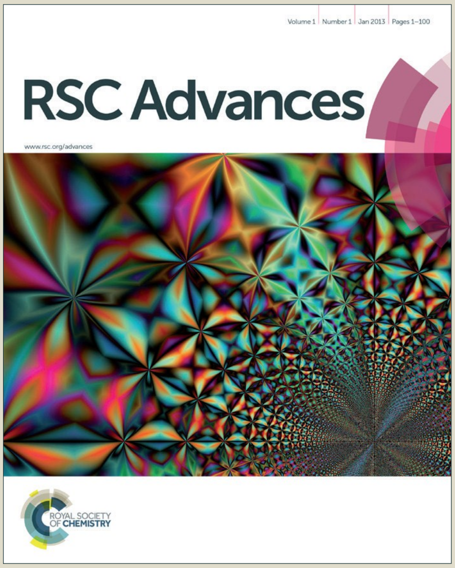

ROYAL SOCIETY OF CHEMISTRY

www.rsc.org/advances

Reduction of graphene oxide gel/carbon nanotube/sulfur cathode material preparation and electrochemical performance

Jianrong Xiao†, Hongzhe Wang*, Yongxuan Hou, Yafang Guo

College of Science, Guilin University of Technology, Guilin 541004, PR China;

Abstract: Reduction of graphene oxide with different reduction degrees was prepared using hydrothermal reduction method at 130–190 °C. X-ray diffraction, scanning electron microscopy, Fourier transform infrared spectrometry, Raman spectroscopy, and electrochemical testing method were conducted to investigate the effect of reduction of graphene oxide gel on the performance of Li–S battery electrochemistry. Results indicate that the reduced graphene oxide gel is a 3D network structure of graphite. The sulfur-based composite material was uniformly embedded, and the loss of the sulfur polymer was suppressed. The reduction degree of graphene oxide (GO) gel increased with increasing water fluid temperatures. By contrast, when the water fluid temperature was 190 °C, the best rate performance of the electrode was observed.

Keywords: Graphene oxide gel; Hydrothermal method; 3D mesh; Li–S battery

1. Introduction

Chemical power source is an energy storage device between super capacitor and capacitors. Lithium sulfur batteries (Li–S), as a high-energy chemical power supply system with high capacity (1675 mAh/g), high specific energy (2600 wh/kg), low cost, no pollution, and many other significant

---

† Corresponding author. E-mail address:xjr@glut.edu.cn(Jianrong Xiao)

* Hongzhe Wang contributed with Jianrong Xiao, and they are both the first author.

advantages[1–3], possess broad application space in the field of mobile electronic devices and other fields. In addition, the lithium battery itself is abundant, low cost, and environmentally friendly; therefore, this battery has attracted considerable attention. However, numerous limiting factors have hindered its extensive practical application. The first limiting factor is the electronic insulation of elemental sulfur; its room temperature conductivity is only about 5×10^{30} S/cm[4–6], which causes the low utilization of active material. Second, the appearance of a high solubility of the sulfur polymer ion Sn^{2-} ($3\leqq n\leqq 6$) in an electrode reaction results in loss of active substances. Moreover, Sn^{2-} shuttling back and forth causes the shuttle between the anode and cathode[7–9]. Third, the end product of electrode reaction is lithium sulfide (Li_2S, Li_2S_2) of insulation, which is removed on the surface of the cathode metal lithium and causes loss of active substances. The apparent volume effect of elemental sulfur in the process of charging and discharging also leads to a decline in battery performance.

To attempt to solve the aforementioned issues encountered by Li–S battery, researchers have conducted excellent works, such as mixing different types of carbon materials (carbon nanotubes [10–14] and graphene [15–16]) and elemental sulfur, to improve the conductive performance of material and the utilization of active material, but many disadvantages still exist. In the electrode reaction process, carbon nanotubes cannot satisfactorily inhibit the dissolution of sulfur polymer ion in the electrolyte, eventually leading to cell cycle performance degradation. To prevent this excessive dissolution, covering a layer of conductive material outside the carbon/sulfur compound material is the best approach. This approach not only improves the conductive performance of sulfur electrode, but also prevents excessive Sn^{2-} diffusion and dissolution. Given the unique structure and excellent physical and chemical properties of 2D [17–18], graphene is often used to improve the performance of carbon/sulfur composites.

In this paper, graphene oxide (GO) was prepared using Hummers method, and then 1 mg/ml GO aqueous solution was made. After GO was ultrasonically dispersed, RGO hydrogel with different reduction degrees was prepared by hydrothermal method at different temperatures, in which the carbon nanotube/sulfur (CNT/S) was dispersed as the base material. Subsequently, the preparation of RGO/CNT/S composites was completed after freeze-drying. The structure, morphology, and electrochemical properties were characterized by X-ray diffraction (XRD), scanning electron microscopy (SEM), and Fourier transform infrared spectrometry (FTIR). LAND test instrument and electrochemical workstation were also employed. Results showed that RGO/CNT/S materials prepared by hydrothermal reduction method and after freeze-drying greatly improved the performance of lithium sulfur battery.

2. **Experiment**

2.1 Preparation of GO samples

GO solution was produced with natural flake graphite (200 mesh, carbon content: 99.9%; Qingdao Hua Tai Lubrication Technology Company, Shandong, China) as raw material through the improved Hummers method[19]. The GO solution was then added with 0.01 mol/l HCl (AR, Nanjing Chemical Reagent Co., Ltd., Jiangsu, China). It was washed to neutral with deionized water (10 MΩ•cm), and GO was obtained after filtration and drying.

2.2 Preparation of reduced graphene oxide (RGO) hydrogel

About 1 mg/ml GO aqueous solution was prepared by a certain amount of the above GO. This solution was uniformly dispersed after 7 h through ultrasonication. Subsequently, the GO aqueous solution with uniform dispersion was obtained. A certain volume of GO water solution was placed into a 50 ml Teflon polytetrafluoroethylene reaction kettle and heated up to 130 °C (heating rate of 5 °C/min), which was maintained for 14 h. When the temperature dropped to room temperature, different reduction degrees of GO hydrogel were produced.

2.3 Preparation of 3D RGO aerogel

Three types of reduction degrees of GO hydrogel were placed in a refrigerator set at −20 °C to precool for 24 h and then were subjected to freeze-drying in a vacuum freeze dryer at −50 °C for 48 h to produce different reduction degrees of 3D RGO aerogels. The samples were marked as follows: RGO-130, RGO-160, and RGO-190. The main preparation process of the samples is shown in Figure 1.

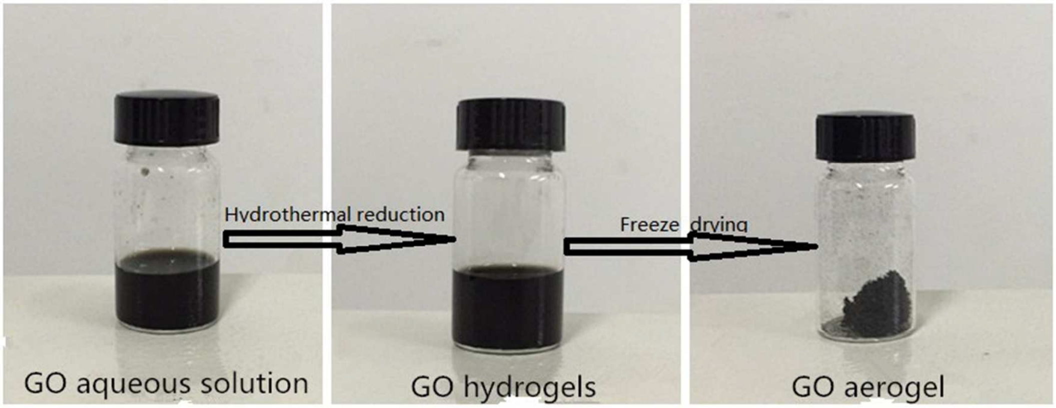

Figure 1 3D reduction oxidation process of graphene aerogel preparation

2.4 Preparation of CNT/S active material

CNT and elemental sulfur (S_8) with a mass ratio of 6:4 were placed in an agate mortar and completely ground for 1 h. They were added into a 50 ml PTFE reaction kettle after stirring well and transferred into a glove box. The box was allowed to stand for 0.5 h to exclude residual air and prevent oxidation of S at high temperature. The reaction was then removed from the glove box and placed in a drying oven at 160 °C for 14 h so that S can be fully fused and spread into the voids of CNTs. After cooling to room temperature, CNT/S active material was produced and marked as CNT/S.

2.5 Preparation of RGO/CNT/S composites,

A certain amount of the CNT/S active material prepared above was removed and dispersed into a certain volume of RGO hydrogel, then was treated ultrasonically at 70 °C for 7 h to increase dispersion on the RGO hydrogel. Samples were placed in a refrigerator at −20 °C for 24 h to precool and then freeze-dried for 36 h to produce RGO/CNT/S composites, which were marked as

RGO-130/CNT/S, RGO-160/CNT/S, and RGO-190/CNT/S.

2.6 Material characterization

The microstructures of samples were observed through field-emission SEM (HITACHIS-4800). Phase and structure analyses were conducted on a MiniFlex600-type XRD (MiniFlex600) with the following test parameters: scan range, 7°–90°; and scan rate, 5.0°/min. FTIR analysis was performed with the Thermo Nicolet NEXUS 670-type FTIR and Raman spectrometer (United States Thermoelectric Company), with a scan range of 350–4000 cm^{-1}. Samples were produced by the KBr pellet.

2.7 Battery preparation and electrochemical performance testing

Battery preparation: The active material, super P li (conductive agent), and PVDF (binder) were uniformly mixed at a mass ratio of 7:2:1. The mixture was scattered in NMP and then ground for 1 h to produce well-proportioned serous, which was painted on the aluminum foil current collector. The collector was placed in a vacuum drying oven at 60 °C for 12 h, and then tailored in a positive plate (with a diameter of 14 mm) and placed in a dry glove box filled with argon (contents of O_2 and H_2O were no more than 0.1 ppm). The composite electrode was the positive electrode, and lithium tablet was the negative electrode; microporous polyethylene was the diaphragm material for the Li–S battery, and electrolyte was 1 mol/l Li TFSI/DME+DOL (volume ratio: 1:1). All of these materials comprise the CR-2025 button cell.

Electrochemical performance testing: The charge–discharge cycle performance tests of batteries were performed using the LAND test instrument at a constant temperature of 27 °C with voltage window set at 1.5–2.8 V. The charge–discharge performance was evaluated with a voltage window set at 1.5–2.8 V (temperature condition: 28 °C), and the charge–discharge specific capacity calculation was based on the quality of the active substance sulfur. Cyclic voltammetry (CV) and alternating current (AC) impedance of the battery were tested on the CHI750E electrochemical workstation with a voltage scanning window of 1.0–3.0 V, a scanning speed of 0.0001 V/s, an impedance test frequency window of 0.01 Hz–100 kHz, and an AC signal amplitude window of 5 mV.

3. Results and Discussion

3.1 Morphology characterization and phase analysis

The XRD patterns of GO and RGO-X (X = 130, 160, 190) are shown in Figure 2. A strong diffraction peak exists near the 2T = 13° with the GO map, which is a GO typical characteristic diffraction peak[20]. Compared with the GO and RGO-X, the high RGO-X diffraction peaks of the spectral lines appear at slightly offset angle, and the positions of the three peaks after shifting are around 2T = 25°. The intensity of the diffraction peak of RGO-130 near 2T = 25° was weakened and gradually enhanced with increasing reduction temperature, whereas the half peak width and interplanar spacing (d) gradually decreased. The corresponding interplanar spacing (d) with GO and RGO-X are listed in Table 1. The data showed that, with increasing hydrothermal reduction temperature, peeling occurs between the layers of RGO, leading interlayer spacing (d) decreased, closer to the ordered graphite interlayer spacing (d=0.335nm), so that the overall structure becomes more similar to the ordered graphite .

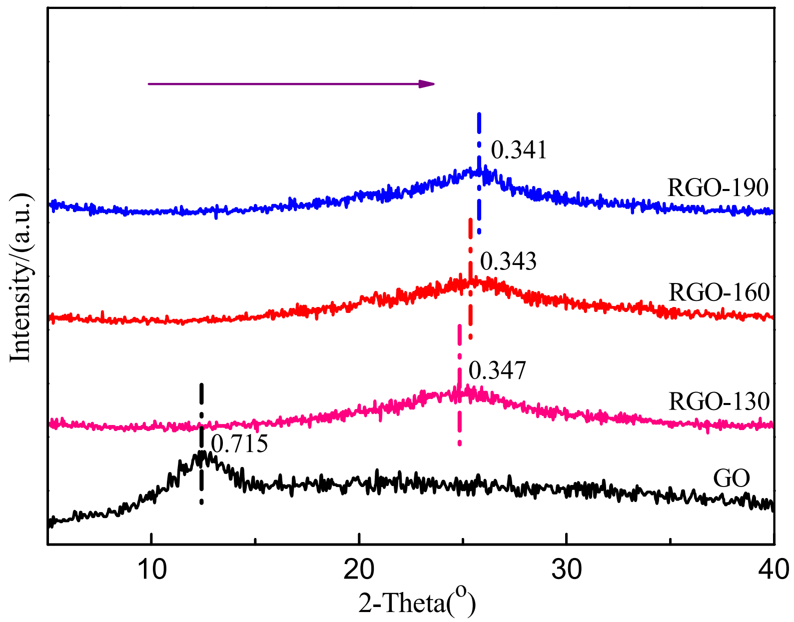

Figure 2 GO and RGO-X (X = 130, 160, 190) XRD spectrum

Table 1 GO and RGO-X (X = 130, 160, 190) interplanar spacing

	2T（°）	d（nm）
GO	11.7	0.715
RGO-130	24.7	0.347
RGO-160	25.0	0.343
RGO-190	25.2	0.341

FTIR spectra of GO and RGO-X (X = 130, 160, 190) are shown in Figure 3. GO contains abundant hydroxyls, carboxyls, carbonyls, epoxy groups, and other functional groups at 1051, 1227, 1632, 1731, 3127, and 3422 cm^{-1} positions, which correspond to C–OH stretching vibration peak, C–O–C stretching vibration peak, β_{OH}, C=O stretching vibration bending vibration peak, V'_{OH} (related to the formation of hydrogen bond), and V_{OH} stretching vibration peak. Interaction between these functional groups overcomes the π–π van der Waals force, which leads to satisfactory dispersion in aqueous solution[21–23]. Compared with GO, the intensities of C–OH, C–O–C, C=O, V_{OH} stretching vibration peaks, and V'_{OH} stretching vibration peak after hydrothermal reaction, which are related to the formation of hydrogen bond in the 3D RGO, are significantly decreased. Higher reduction temperature results in more evidently decreased stretching vibration peak of each functional group. This phenomenon renders the structure of carbon atoms similar to the initial graphite[24] and enhances the entire electrical conductivity.

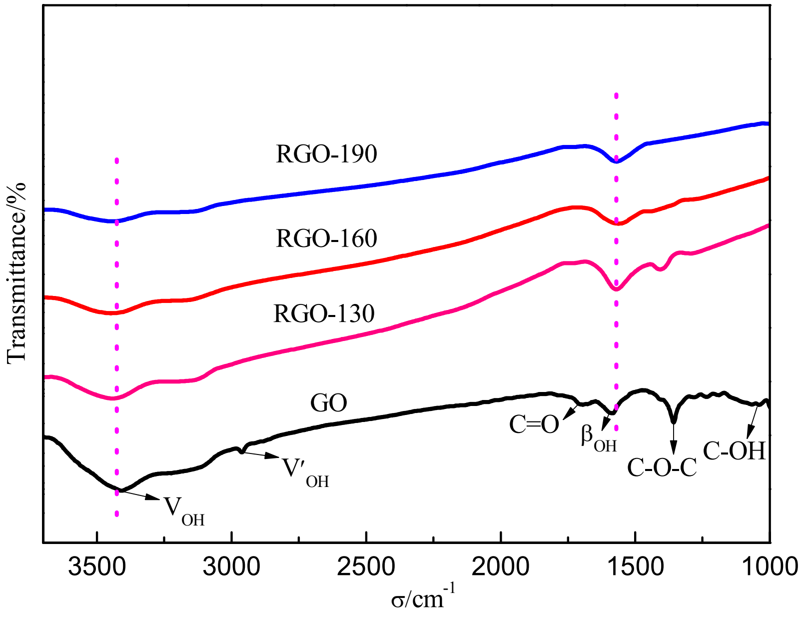

Figure 3 FTIR spectra of GO and RGO-X (X = 130, 160, 190)

GO and RGO-X (X=130160190) Raman spectra shown in Figure 4, as can be seen, all samples were produced Raman characteristic peaks in 1353cm^{-1} and 1593cm^{-1}, respectively, corresponding to D band and G band. D band and G band intensity ratio (I_D/I_G) determines the degree of GO was reduced, the greater of I_D/I_G value the lower the degree of order of RGO, and the degree of order may be caused by the defects of the sample [25]. The Raman spectra of all samples were fitted with fit Peak software. After taking the integral, I_D/I_G values before and after hydrothermal reduction were obtained. At the same time, the conductivity was tested by four probe method before and after reduction, obtained the electrode conductivity (κ) values, I_D/I_G value and κ values are listed in Table 2. The data in the table shows that with the increase of hydrothermal temperature, the value of I_D/I_G and κ value was increased. The increase of I_D/I_G value is caused by defects increased in the sample, Increasing κ value is due to the functionalized conjugate is weakened in RGO, which is in agreement with the results of FTIR spectra in Figure 3.

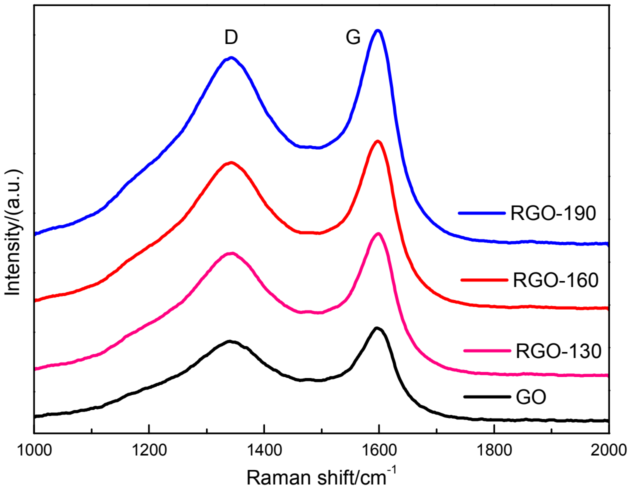

Figure 4 Raman spectra of GO and RGO-X (X = 130,160,190)

Table 2 I_D/I_G values and the conductivity for the electrode

	GO	RGO-130	RGO-160	RGO-190
I_D/I_G	1.27	1.46	1.57	1.63
κ（S/cm）	4.976481E-3	2.48824E-2	2.9858886E-2	3.4835367E-2

SEM images of GO and different reduction degrees of RGO-X (X = 130, 160, 190) gel are shown in Figure 5. As can be seen from Figure 5a, deep rolling folds on the surface of GO and interlayer reunion phenomenon are observed, but the overall appearance has no fixed structure. Figure 5b presents that at a reduction temperature of 130°C, the GO lamella structure is faintly visible, and the interlayer reunion phenomenon evidently decreases, but the overall appearance has no fixed structure [26]. At a reduction temperature of 160°C, the GO lamellar structure is more apparent, and the interlayer reunion phenomenon largely disappears; a 3D structure is also present as shown in Figure 5c. In Figure 5d, at a reduction temperature of 190 °C, the GO lamella structure is more apparent, and the samples maintain a 3D network structure.

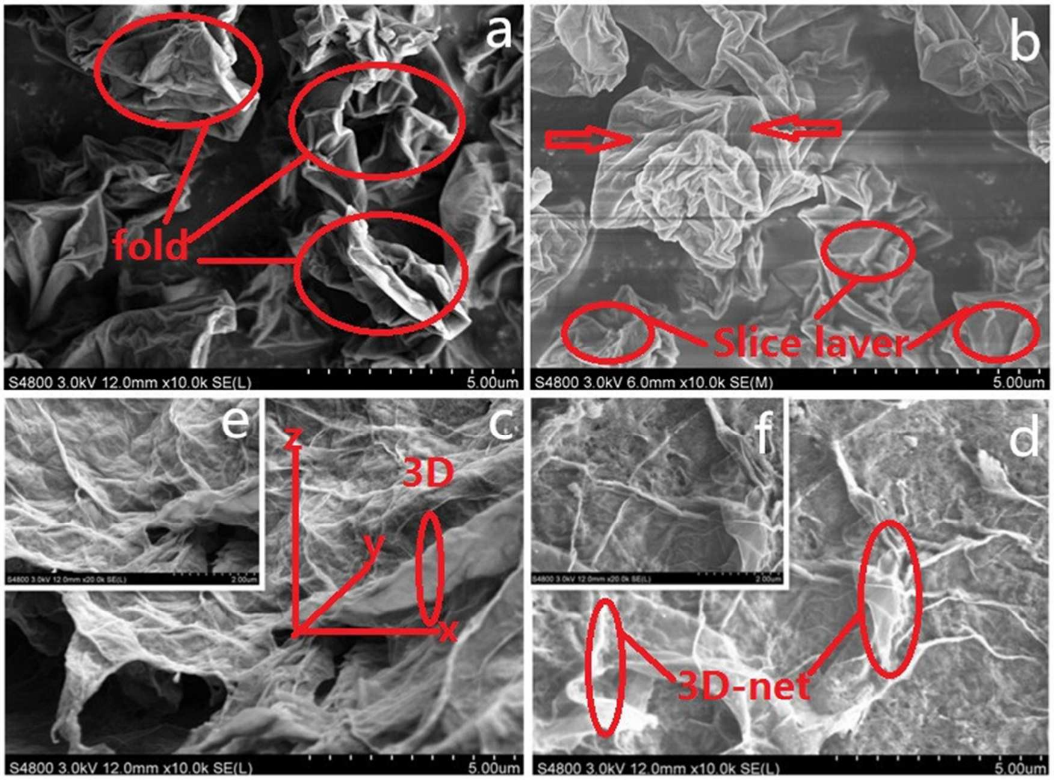

Figure 5 SEM images of GO and RGO-X (X = 130, 160, 190)
(a) GO, (b) RGO-130, (c) RGO-160 (10k), (d) RGO-190 (10k), (e) RGO-160 (20k), (f) RGO-190 (20k)

3.2 Electrochemical properties

Figures 6a and 6b show the first and third CV graphs of RGO-X/CNT/S composite electrode, respectively, and Figure 6c presents the first and third CV curve graph of CNT/S composite electrode. All electrodes have two reduction peaks and an oxidation peak, which is a typical electrochemical behavior of lithium sulfur batteries. After the first loop, the two reduction peaks of CNT/S electrode and RGO-X/CNT/S electrode are both around 2.0 V (S42-→S2-) and 2.25 V (S8→S42-); the positions of the reduction peaks that correspond to RGO-130/CNT/S and RGO-190/CNT/S are slightly higher than RGO-160/CNT/S electrode. This result is attributed to the viscosity of S8, which is lowest at the reduction temperature of 160 °C; thus, the cladding structure cannot be formed well with 3D RGO gel. After three loops, the reduction peaks of RGO-X/CNT/S composite electrode overlap, which indicates that the number of oxygen-containing functional groups decreased under the high reduction temperature causing the increase of the overall conductivity and the rate of electron transport in the electrode reaction, thereby increasing the utilization of active material S8. In addition, after the first cycle, the SEI films of the three composite electrodes are basically formed, which also render the electrode structure stable. In Figure 6c, CNT/S electrode without RGO gel cannot effectively inhibit the "shuttle" effect[7,11,12], resulting in loss of many active materials. This phenomenon leads to unchanged reduction peak position of electrode after three loops. The above CV analysis shows that RGO-190/CNT/S composite electrode has better electrochemical behavior at the reduction temperature of 190 °C.

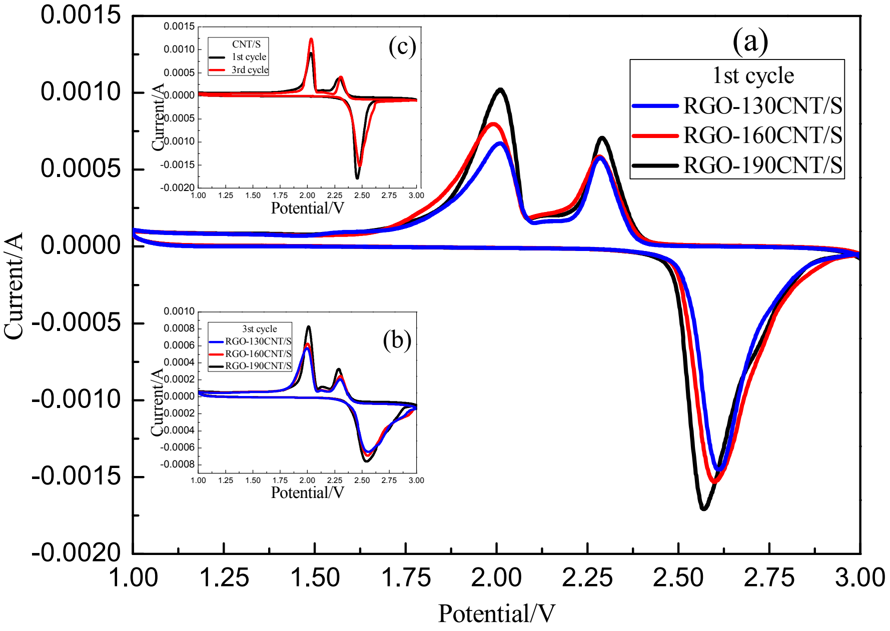

Figure 6 Cyclic voltammetry (CV) curves of different samples
(a) RGO-X/CNT/S (1st), (b) RGO-X/CNT/S (3rd), and (c)CNT/S

The first charge and discharge performance of different electrodes at the current density of 200 mA/g are shown in Figure 7. Each electrode has two discharge platforms; this finding agrees to the

CV curves in Figure 6, which is a typical discharge platform curve of Li–S battery. In Figure 7b, the first specific discharge capacity of CNT/S electrode is 907.1 mAh/g at the current density of 200 mA/g, whereas in Figure 7a the first specific discharge capacities of RGO-X (130, 160, 190)/CNT/S increase to 1081.7, 1181, and 1297.4 mAh/g, respectively, and the first coulomb efficiencies are 83.8%, 91.7%, and 91.2%. The batteries show a better charging–discharging retention rate and repeat utilization of active materials. On the one hand, this result is due to the conductivity of the RGO gel. The conductivity enhanced with increasing reduction temperature, speeding up the electronic conductivity of the composite electrode, thus more active materials are involved in the electrode reaction. On the other hand, the 3D network structure of RGO gel can easily fix active materials, so the "shuttle" effect was suppressed to a certain degree and loss of active materials in the electrode reaction was reduced.

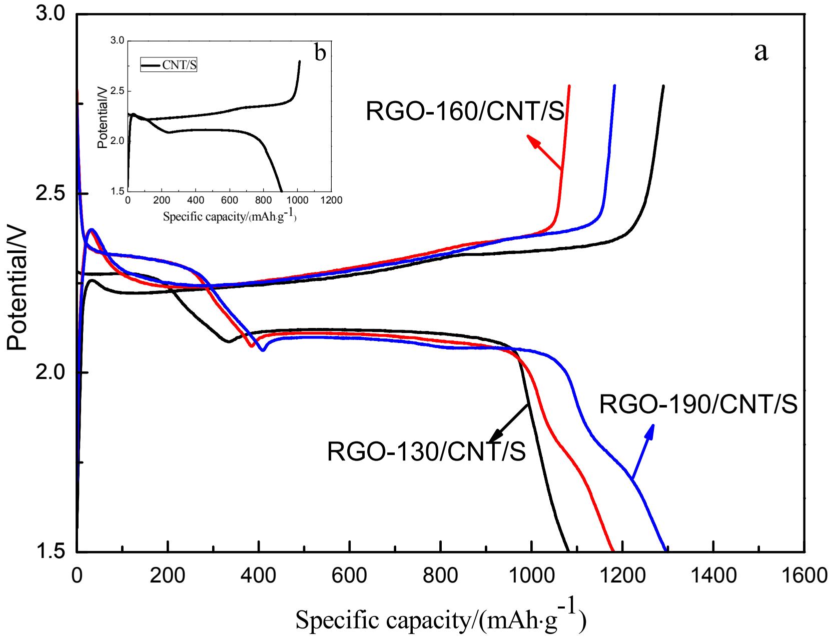

Figure 7 (a) RGO-X/CNT/S and (b) CNT/S cycle discharge/charge voltage profiles at a current density of 200 mA/g

Figure 8 shows the circulating performance of different composite electrodes at a current density of 400 mA/g. The first specific discharge capacity of CNT/S electrode was 984 mAh/g and became 679.1 mAh/g after 50 loops. The capacity attenuation was extremely severe, the retention rate was only 69%, and the coulomb efficiency remained at around 80%. The discharge curves of RGO-X (130, 160, 190)/CNT/S electrodes were smooth, and their specific capacity was larger than the CNT/S electrodes. The capacity retention ratios of the composited RGO were 81.4%, 82.9%, and 84.6%, and the coulomb efficiencies were maintained at more than 90%. RGO gel greatly improved the cycle performance of the electrode, which was mainly due to the RGO gel with a strong physical adsorption function to fix active substances effectively and prevent excessive dissolution of polysulfide lithium in the electrolyte. RGO gel is slightly different under different reduction temperatures. Data showed that higher reduction temperature results in more superior performance of RGO/CNT/S electrode. This superior performance is due to the conductivity of the composite materials, which further enhances with increasing reduction temperature causing the acceleration of kinetic rate of electrochemical reaction. RGO gel showed evident layer structure under higher reduction temperature, which made it easier for active materials to disperse evenly on the RGO gel surface and then improve the utilization of active material.

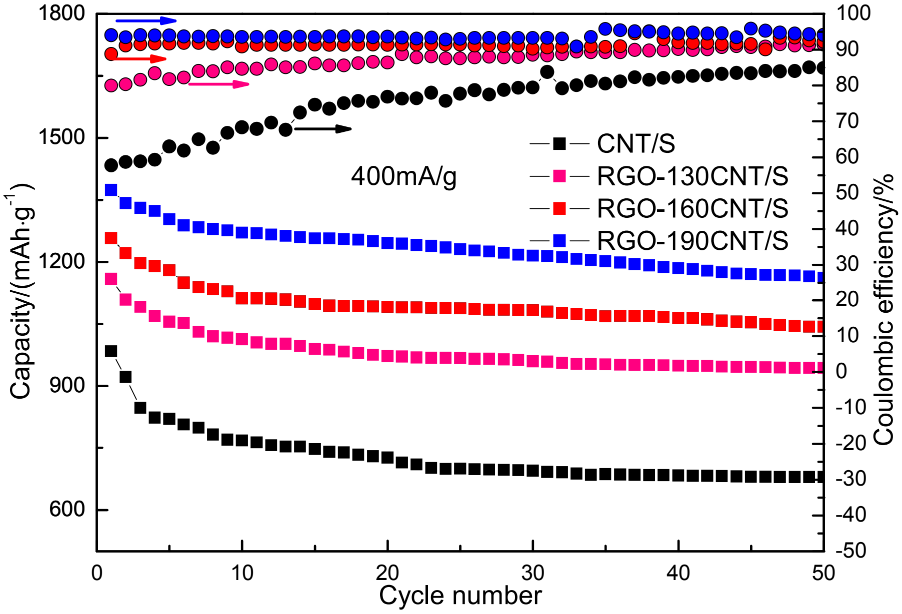

Figure 8 Cycle performance and coulomb efficiency of different composites at a current density of 400 mA/g

Figure 9 presents the comparison of rate capacities of electrodes. All of the electrodes were tested with the following current densities: 100 mA/g→200 mA/g→400 mA/g→800 mA/g→100 mA/g. When the current density was 100 mA/g, the discharge capacity of CNT/S was 980 mAh/g. After 50 laps, the reversible specific capacity was 384 mAh/g, and the capacity retention rate was only 39.2%. The CNT/S electrode exhibited a poor reversibility at a high current density condition. The reversible specific capacity of RGO-X (X = 130, 160, 190)/CNT/S electrode were 689, 846, and 934 mAh/g, respectively, after 50 cycles. The capacity retention rates were60%, 66.8%, and 68%, respectively, which showed a good reversibility. This finding is due to the 3D network structure of RGO gel, which can effectively fix active substances. This structure can also be used as an elastic buffer and weaken the influence of volume effect on the electrode structure. Data also showed that the ratio properties of the electrode rose with increasing reduction temperature; the best rate performance of the electrode was observed at the reduction temperature of 190 °C. This is due to the increase in reduction temperature results in increased RGO gel layer of a specific surface area[24];

this phenomenon is easy for the active substance to be infiltrated by the electrolyte so that more lithium sulfide is reduced.

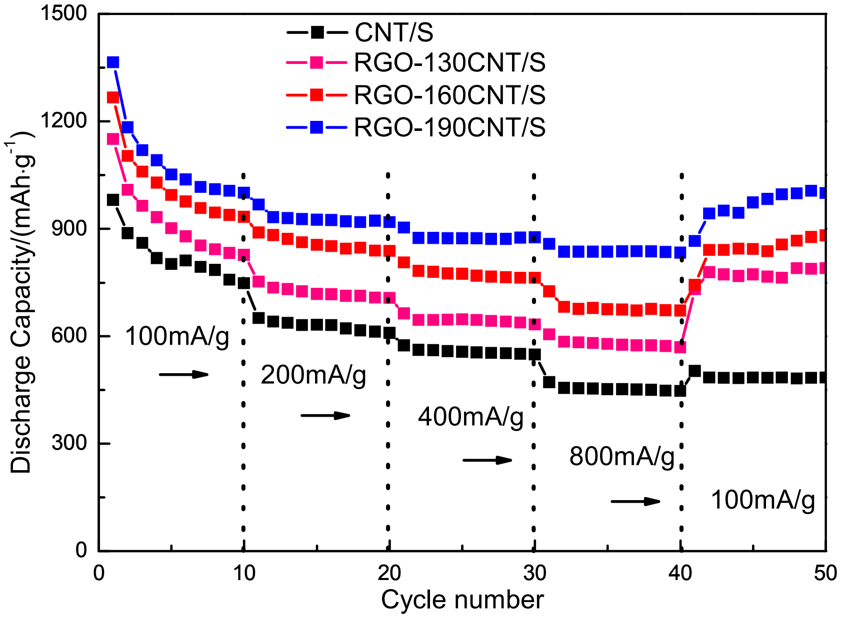

Figure 9 Rate performance of CNT/S and RGO-X/CNT/S cathode

The electrochemical impedance spectra (EIS) of different electrodes before and after the cycle are shown in Figure 10. Cycle condition is charge and discharge 10 times under the current density of 100 mA/g. The EIS curve is composed of three parts. The curve and real axis Z′ intercepts are the intrinsic impedance of batteries (active material resistance, electrolyte resistance, and current collector interface resistance). Marker represents R1, and the half arc diameter of the high frequency region corresponds to the charge transfer resistance (R2). The low frequency region for a horizontal axis and a 45 degree diagonal (Warburg impedance, marked as ZW) correspond to the diffusion impedance of Li^+ in the electrolyte [27–28]. ZView software was used to fit the electrochemical impedance spectra of different electrodes before and after cycling. R1, R2, and ZW values of different electrodes were obtained and are listed in Table 3. Table 3 shows that after 10 cycles, the R1, R2, and ZW resistance of all the electrodes are less than before, and this is consistent with the impedance spectra. This finding is attributed to the 10 cycles of the electrodes, which resulted in active substance infiltration by electrolytes and reduction of Li^+ diffusion resistance in electrolytes. The data also showed that the impedance value of the RGO-X/CNT/S electrode was less than that of the CNT/S electrode. Meanwhile, the resistance decreased gradually with increasing reduction temperature. The electrodes showed the best electrochemical performance at a reduction temperature of 190°C. This performance is due to higher reduction temperature, which results in better conductive properties of RGO gel and promotes the rapid transmission of electrons in composite materials. In addition, the 3D mesh structure is convenient for the rapid diffusion of the electrolyte, reducing the resistance of the electrolyte ions in the penetration process.

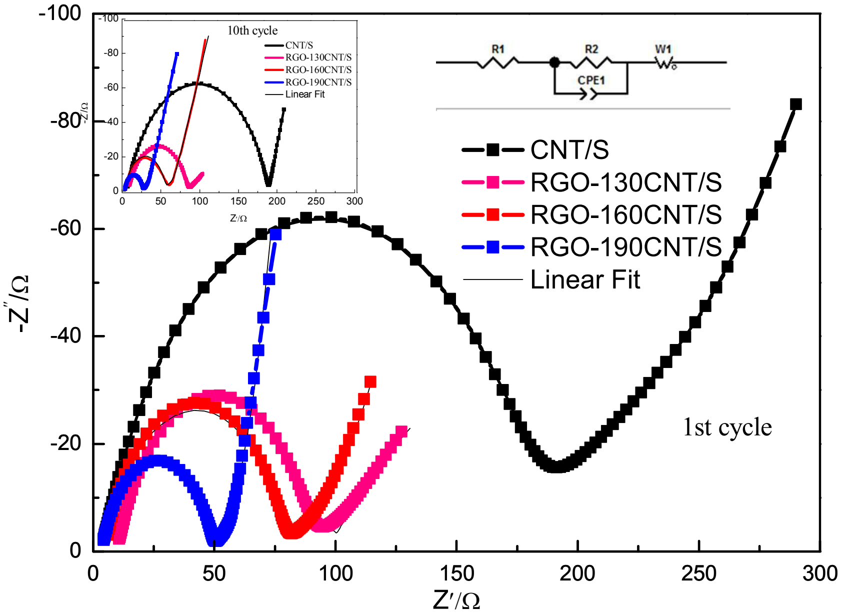

Figure 10 Impedance plots before and after the cycle for CNT/S and RGO-X/CNT/S cathode

Table 3 Kinetic parameters of electrode

Sample	Stage	R1(Ω)	R2(Ω)	Zw(Ω)
CNT/S	Cycle before	22.96	107.4	74.4
	After 10 cycles	26.21	88.2	62.23
RGO-130/CNT/S	Cycle before	8.631	75.99	42.68
	After 10 cycles	8.282	75.12	34.22
RGO-160/CNT/S	Cycle before	4.748	72.57	44.35
	After 10 cycles	3.616	50.72	30.79
RGO-190/CNT/S	Cycle before	3.669	45.39	20.83
	After 10 cycles	3.414	22.78	19.72

4. Conclusion

(1) Hydrothermal reduction combined with freeze-drying method can successfully prepare 3D structure of RGO aerogel. When the temperature rose to 160 °C, the degree of order was enhanced and the significant lamellar structure of the RGO gel showed a 3D network structure.

(2) When RGO/CNT/S was used as Li–S battery cathode material, the battery exhibited good electrochemical performance compared with the CNT/S electrode. Higher reduction temperature results in greater degree of GO reduction, better 3D RGO gel performance, and more suitable elastic buffer to adapt to changes in electrode volume.

Conflict of Interests

The authors declare that there is no conflict of interests regarding the publication of this paper.

Acknowledgments

The authors are grateful to the National Natural Science Foundation of China (Grant No. 11364011), the Guangxi Natural Science Foundation (Grant No. 2015GXNSFAA139004) and the Innovation

Project of Guangxi Graduate Education (Grant No. YCSZ2015164).

References

[1] N. Jayaprakash, J. Shen, S. S. Moganty, A. Corona, and L. A. Archer, *Angew. Chem. Int. Edit.*, 2011, **123**, 6026-6030.

[2] C. Wang, J. J. Chen, Y. N. Shi, M. S. Zheng, and Q. F. Dong, *Electrochimica Acta*, 2010,**55,** 7010-7015.

[3] Q. Wang, J. Pan, M. Li, Y. Luo, H. Wu, L. Zhong, and G. H. Li, *J. Mater. Sci. Technol.*, 2015, **31**, 630-633.

[4] A. K. Geim and K. S. Novoselov, *Nat. Mater.*, 2007, **6**, 183-191.

[5] N. D. Mermint, *Phys. Rev.*,1968, **176**, 250-254.

[6] X. Ling, and J. Zhang, *Acta Phys-Chim. Sin.*, 2012, **28,** 2355-2362.

[7] X. L. Ji, K. T. Lee, L. F. Nazar, *Nat. Mater.*, 2009,**8**, 500-506.

[8] L. F. Xiao, Y. L. Cao, J. Xiao, B. Schwenzer, M. H. Engelhard, L. V. saraf, Z. Nie,G. J. Exarhos, and J. Liu, *Adv. Mater.*, 2012, **24**,1176-1181.

[9] X. L. Ji, and L. F.Nazar , *J. Mater. Chem.*, 2010, **20**: 9821-9826.

[10] S. C. Han, M. S. Song, H. Lee, H. S. Kim, H. J. Ahn, and J. Y. Lee, *J. Electrochem. Soc.*, 2003 **150**, A889-A893.

[11] W. Zheng, Y. W. Liu, X. G. Hu, and C. F. Zhang, *Electrochim. Acta,* 2006, **51**, 1330-1335.

[12] L. X. Yuan, H.P. Yuan, X.P. Qiu, L. Q. Chen, and W. T. Zhu, *J. Power Sources,* 2009, **189**,1141-1446.

[13] J. J. Chen, X. Jia, Q. J. She, C. Wang, Q. Zhang, M. S. Zheng, and Q.F. Dong, *Electrochim. Acta*, 2010, **55**, 8062-8066.

[14] M. W. Xu, C. J. Cheng, Q. Q. Sun, S. J. Bao, Y. B. Niu, H. He, Y. T. Li, and J. Song, *RSC Adv.*, 2015, **5**, 56686-56686.

[15] G. Y. Xu, B. Ding, P. Nie, H. J. Luo, and X. G. Zhang, *Acta Phys. -Chim. Sin.*, 2013, **29** , 546-552.

[16] S. Aziz, J. Q. Zhao, C. Cain, and Y. Wang, *J Mater. Sci. Technol.*, 2014, **30**, 427-433.

[17] L. P. Xue, M. B. Zheng, C. F. Shen, H. L. Lu, N. W. Li, L. J. Pan, and J. M. Cao, *Chinese J. Inorg. Chem.*, 2010, **26**, 1375-1381.

[18] M. Ciszewski, A. Mianowski, and G. Nawrat, *J Mater Sci: Mater Electron.*, 2013, **24**, 3382-3386.

[19] W. S. Hummers, and R. E. Offeman, *J. Am. Chem. Soc.*, 1958,**80**,1339.

[20] D. R. Dreyer, S. Park, C. W. Bielawski, and R. S. Ruoff, *Chem. Soc. Rev.*, 2010, **39**, 228-240.

[21] H. K. Jeong, Y. P. Lee, Rob J. W. E. Lahaye, M. H. Park, K. H. An, I. J. Kim, C. W. Yang, C. Y. Park, R. S. Ruoff, and Y. H. Lee, *J. Am. Chem. Soc.*, 2008, **130**, 1362-1366.

[22] W. Cai, R. D. Piner, F. J. Stadermann, S. Park, M. A. Shaibat, Y. Ishii, D. Yang, A. Velamakanni, S. J. An, M. Stoller, J. An, D. Chen, and R. S. Ruoff, *Science*, 2008, **321**, 1815-1817.

[23] A. Barinov, O. B. Malcioglu, S. Fabris, T. Sun, L. Gregoratti, M. Dalmiglio, and M. Kiskinova, *J. Phys. Chem. C*, 2009, **113**, 9009-9013.

[24] S. Stankovich, D. A .Dikin, R. D. Piner, K. A. Kohlhaas, A. Kleinhammes, Y. Y. Jia, Y. Wu, S. T. Nguyenb, and R. S., Ruoff, *Carbon*, 2007, **45**, 1558-1565.

[25] Thomsen, C, Reich, S. Phys. Rev. Lett. 2000, 85: 5214.

[26] H. Bi, K. Yin, X. Xie, Y. Zhou, N. Wan, F. Xu, F. Banhart, L. Sun, and R. S. Ruoff, *Adv. Mater.,* 2012, **24**, 5124-5129.

[27] L. X. Yuan, X. P. Qiu, L. Q. Chen, and W. T. Zhu, *J Power Sources*, 2009, **189**,127-132.

[28] K. L. Zhu, J. H. Tian, L. P. Liu, Q. W. Tang, X. M. Yu, Y. M. Zhu, and Z. Q. Shan, *RSV Adv.*, 2013, **3**, 13149-13155.